ACS APPLIED MATERIALS & INTERFACES

Research Article

www.acsami.org

Architectured Morphologies of Chemically Prepared NiO/MWCNTs Nanohybrid Thin Films for High Performance Supercapacitors

Girish S. Gund,[†] Deepak P. Dubal,[‡] Sujata S. Shinde,[†] and Chandrakant D. Lokhande*,[†]

[†]Thin Film Physics Laboratory, Department of Physics, Shivaji University, Kolhapur, 416004 Maharashtra, India

[‡]Institut für Chemie, AG Elektrochemie, Technische Universität Chemnitz, D-09107 Chemnitz, Germany

Supporting Information

ABSTRACT: The preparation of nanostructured metal oxide decorated on multiwalled carbon nanotubes (MWCNTs) nanohybrid films through simple, scalable, additive-free, binderless, and cost-effective route has fascinated significant attention not only in fundamental research areas but also its commercial applications, in order to reduce the growing environmental pollution and the cost of electrode fabrication. Here, we report the fabrication of highly flexible electrode with NiO/MWCNTs nanohybrid thin films directly on stainless steel substrate using successive ionic layer adsorption and reaction (SILAR) method. The impact of ratio of adsorption and reaction cycles on structural, surface areas and electrochemical properties of NiO/MWCNTs nanohybrids was investigated. X-ray diffraction measurements confirm the hybridization and face centered cubic (FCC) crystal structure of NiO in NiO/MWCNTs nanohybrids. In addition, these nanohybrids exhibit excellent surface properties such as uniform surface morphology, good surface area, pore volume, and uniform pore size distribution. The electrochemical tests demonstrate the highest specific capacitance of 1727 F g^{-1} at 5 mA cm^{-2} of current density with 91% capacitance retention after 2000 cycles. In addition, the Ragone plot confirms the better power and energy densities for all NiO/MWCNTs nanohybrids. The attractive electrochemical capacitive activity revealed by NiO/MWCNTs nanohybrid electrode proposes that it is an auspicious respondent for future energy storage application.

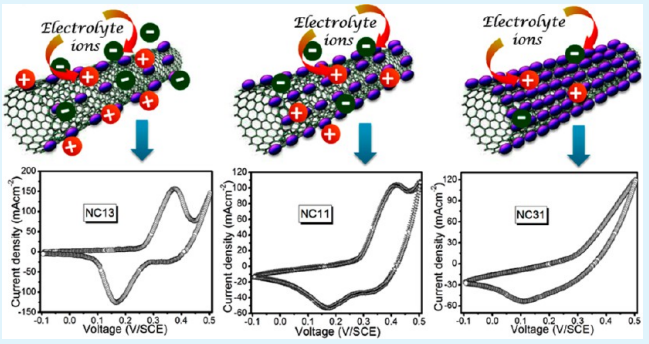

KEYWORDS: *nanostructured hybrids, nickel oxide, multiwalled carbon nanotubes, mass loading, highly flexible solid-state symmetric supercapacitor*

1. INTRODUCTION

The pure, inexpensive and trustworthy energy employment approach is a foundation of global growing economical success as the progressive industrialization. Solar-, wind-, and water-based energy generation are only some examples of the options. So the only increasing efficiency is not adequate. Therefore, the burning need of maturity and implementation of efficient energy storage devices are crucial to harness the alternative energy produced, since the sun does not shine during the night, wind does not blow on demand, and water does not fall and run incessantly. Accordingly, the noteworthy and challenging progression is concentrated for the practical and safe consumption of this technology and will be advanced as a consequence of new developments in nanotechnology.

A supercapacitor, also known as ultracapacitor or electrochemical capacitor, is an assuring energy storage device, which can act as a gap bridging function between batteries and conventional capacitors.[1] The charge storage mechanisms on which a supercapacitor works are surface ion adsorption (electric double layer capacitance, EDLC) and redox reactions (pseudocapacitance). In comparison to batteries, supercapacitors reveal a gifted set of features such as high power density, fast rates of charge discharge, reliable cycling life, and safe operation. However, EDLC (carbon based) supercapacitors exhibit very low energy densities, which is restricted through the finite electrical charge separation at the interface of electrode materials and electrolyte, and the accessibility of surface area. As a result, efforts to increase the energy densities of supercapacitors have included the use of improved pseudocapacitance electrode materials, furnished by nanostructured transition metal oxides and conducting polymers bearing the cost of high power density and chemical stability, which are the consequence of phase changes and faradic reactions in it.[2]

Coalesce of charge storage mechanisms, EDLC and pseudocapacitance, called hybrid supercapacitors, render the superior features of the device. The multiwalled carbon nanotubes (MWCNTs), among the other EDLC electrode materials, attracted major interest owing to their auspicious characteristics such as excellent electrical conductivity, high

Received: October 8, 2013
Accepted: February 18, 2014
Published: February 18, 2014

dx.doi.org/10.1021/am404422g | ACS Appl. Mater. Interfaces 2014, 6, 3176−3188

surface area and mesoporous network, good mechanical strength and flexibility, and chemical stability. Moreover, MWCNTs allow a conducting pathway to assist a fast electrochemical kinetic process during high current density charge/discharge in a hybrid supercapacitor. The different electrode materials, such as metal oxides (MnO_2, Co−Ni oxide, etc.) and conducting polymers (polyaniline, polypyrrole, etc.), designed on MWCNTs have exposed superior electrochemical behavior. In addition, the electrochemical performance of a hybrid supercapacitor is significantly altered through the mass loading of material on the MWCNTs. In all transition metal oxides, ruthenium oxide (RuO_2) has been widely examined as active electrode material owing to its high theoretical capacitance (~2000 F g^{-1}) in a wider applied potential window of ~1.4 V; however, the expensive and toxic nature of ruthenium is inadequate for commercialization.[3] Nickel-based materials such as nickel oxide (NiO) and hydroxide ($Ni(OH)_2$) are excellent pseudocapacitive electrode materials, among the other metal oxides, due to their high electroactivity and simple processing. Additionally, NiO and $Ni(OH)_2$ have very high theoretical capacitances larger than 2584 F g^{-1}, are low cost, are in natural abundance, are environmentally friendly, and show the possibility of enhanced performance through different preparative methods.[4−7] Conversely, the poor electrical conductivity and low cycle life of pseudocapacitive NiO restricted their practical applications. Accordingly, the design of a MWCNTs wall with the NiO in NiO/MWCNT nanocomposite electrode may offer, high surface area with a conducting channel to deliver the fast electrochemical kinetic process, and good chemical stability to NiO nanomaterials through the $\pi-\pi$ bonding between side wall of MWCNTs and NiO.[8,9] Additionally, NiO/MWCNTs hybrid nanocomposite will provide one-dimensional (1D) nanostructure, which maximizes the active materials utilization ratio and decreases the diffusion length significantly, owing to high specific capacitance and excellent cycling stability.

Currently, the preparation of additive-free and binderless electrode to avoid the "dead surface" in traditional slurry-derived electrode architectures has become a hot topic in the field of materials research which allows more efficient charge and mass exchange. The traditional slurry derived route for NiO/carboneous material composite was followed by Yuan et al. (NiO/activated carbon (AC)),[10] Lee et al. (NiO/CNT),[11] Su et al. (NiO/CNT),[12] Lin et al. (NiO/CNT),[13] and so forth. While the additive-free and binderless path has adopted by Salunkhe et al. (Ni−Co hydroxide/MWCNT composite through chemical bath deposition (CBD) method),[14] Dubal et al. ($Ni(OH)_2$/MWCNT composite through successive ionic layer adsorption and reaction (SILAR) method),[15] Zhao et al. (MnOx/CNT composite through electrodeposition),[16] and so forth. Among these, SILAR is a soft chemical solution method, whose basic building blocks are ions instead of atoms/molecules. So, the layer-by-layer assembly of pseudocapacitive (NiO) layer and conducting MWCNTs layer offer superior route to boost the electrochemical properties. Consequently, SILAR furnishes outstanding material utilization efficiency, affords fine control of the film thickness of composite and mass loading of pseudocapacitive material on the MWCNTs, and is explicitly suitable for large area deposition with the low cost technique. Additionally, oxidation and corrosion of metallic substrates can be easily prevented as a consequence of low temperature deposition.

The present investigation is focused on the synthesis and the electrochemical properties of MWCNTs integrated with different nanostructures of NiO using SILAR method. The effect of ratio of adsorption and reaction cycles on structural, surface areas and electrochemical properties of NiO/MWCNTs nanohybrids was investigated. This method is more controllable and efficient in order to alter the nanostructures and mass loading. The fine controlled nanostructures designed on the walls of MWCNT in the nanohybrids can improve the electrical conductivity through offering good conductive paths, which has given fruition of enhanced electrochemical properties. Additionally, highly flexible solid state supercapacitor has been fabricated based on the NiO/MWCNTs nanohybrid electrode. Moreover, these types of simply fabricated supercapacitors, connected in series, are successfully used to glow the commercial light emitting diode (LED).

RESULTS AND DISCUSSION

Film Formation and Reaction Mechanism. The growth kinetics of thin film formation in the SILAR method is of two types: (i) ion-by-ion growth where the deposition process involves the ion-by-ion deposition at nucleation sites on the immersed surfaces and (ii) nucleation occurs via adsorption of the colloidal particles, and growth occurs as a consequence of surface coagulation of these particles, giving a thin and adherent film,[17] which is referred as cluster-by-cluster growth of the film.

$Ni(OH)_2$ nanoparticles were decorated on the walls of MWCNTs through the electrostatic adsorption and reaction among the cations and anions at the surface of MWCNTs. In brief, the well dispersed functionalized MWCNTs solution into the deionized water was prepared using an ultrasonicator. The immersion of FSS substrates into this solution leads to the adsorption of MWCNTs onto the substrate surface as a consequence of interaction between unbalanced forces on the substrate surface and the functional groups on the MWCNTs, which is schematically shown in Supporting Information Figure S1. Similarly, Lee et al.[18] have prepared CNT binder-free deposition on the different types of substrates using the layer-by-layer method. The second beaker containing 0.05 M $NiSO_4$ was used as a source of nickel, and aqueous ammonia (NH_4OH) solution (25% extrapure) was added with constant stirring to make it alkaline. Primarily, while adding aqueous ammonia solution into nickel sulfate, the ionic product of $Ni(OH)_2$ surpassed the solubility product, and the solution turned to turbid as a result of the greenish murky precipitation of $Ni(OH)_2$ according to the following proposed reaction:

$$NiSO_4 + NH_4OH \rightarrow Ni(OH)_2 \downarrow + 2NH_4^+ + SO_4^{2-} \quad (1)$$

Further addition of ammonium hydroxide dissolves the precipitate and forms the $Ni(NH_3)_q^{2+}$ complex ion by replacing OH^- ligands around Ni^{2+}, q = 1−4, with 4 being the most stable coordination number.[19] As a result of complex formation, the solution color changes from greenish murky to clear and transparent blue, which can be justified through the following reaction:

$$Ni(OH)_2 + 4NH_4^+ \rightarrow Ni(NH_3)_4^{2+} + 2H_2O + 2H^+ \quad (2)$$

When the substrate was dipped in the above solution, the $Ni(NH_3)_4^{2+}$ ions in the solution were adsorbed on the walls of the MWCNTs as the initial choice, due to the electrostatic

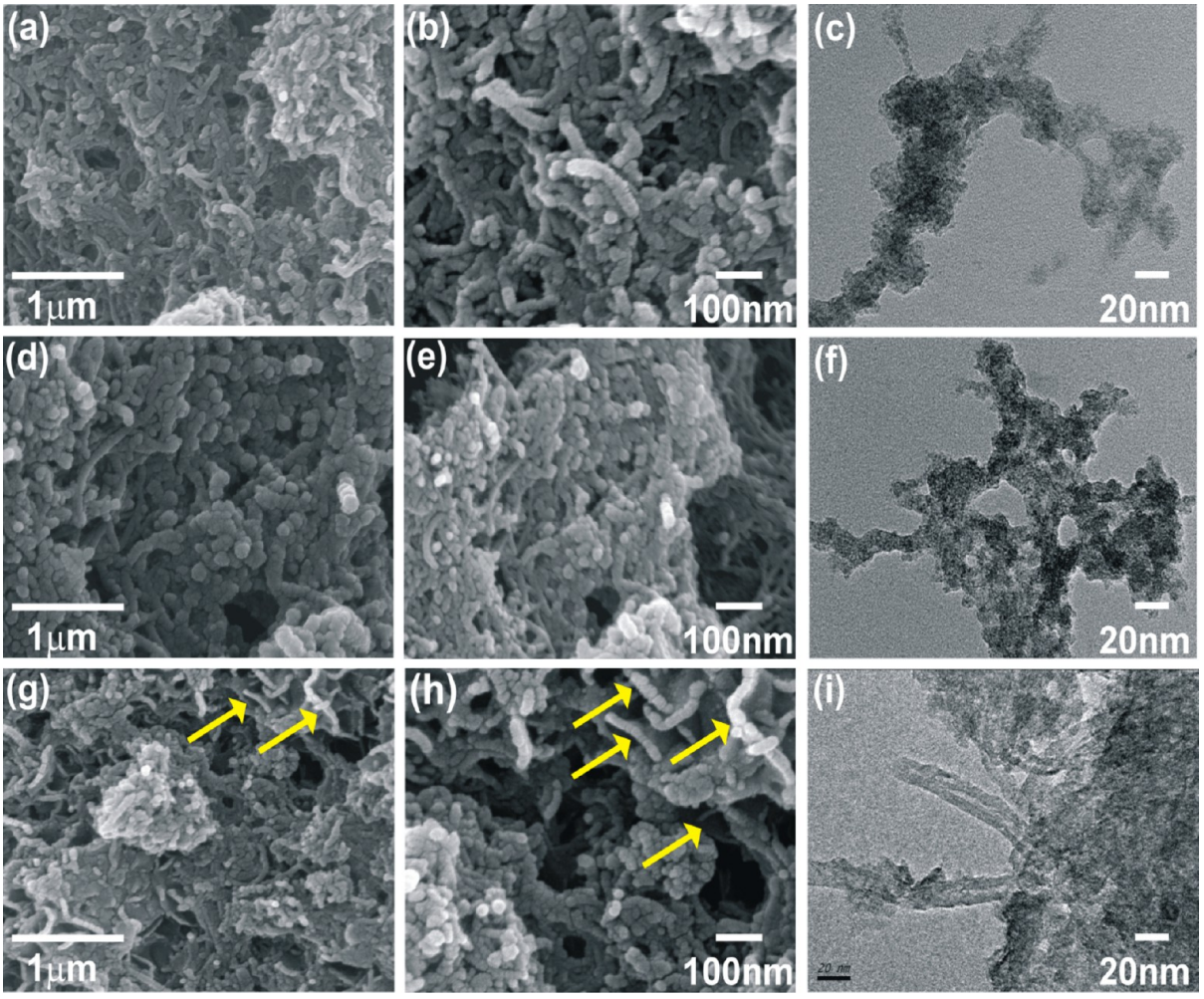

Figure 1. (a, b, d, e, g, h) FE-SEM images and (c, f, i) TEM micrographs of (a–c) NC13, (d–f) NC11, and (g–i) NC31 samples (yellow arrows indicate the nanoflakes).

force of attraction between the $Ni(NH_3)_4^{2+}$ ions and the functionalized MWCNTs.

The substrate is then dipped in dilute H_2O_2 solution maintained at 333 K, to alter the nickel complex into $Ni(OH)_2$ by the reactions, which can be explained as follows:

$$Ni(NH_3)_4^{2+} + 2OH^- \rightarrow Ni(OH)_2 + 4NH_3\uparrow \quad (3)$$

Here, the dilute H_2O_2 solution acts as a source of hydroxyl ions upon heating at 333 K. This step accomplished a single SILAR cycle. Such a cycle was reproduced several times (80) to obtain the film of optimum thickness. Lastly, the $Ni(OH)_2$/MWCNT thin film was rinsed with double distilled water several times to remove loosely bound and unreacted species. To assemble the mass loading of $Ni(OH)_2$ onto the MWCNTs, the single cycle was composed of different layers of MWCNTs adsorption and ion adsorption followed by oxidation reaction (means MWCNT and $Ni(OH)_2$) as 3:1, 1:1, and 1:3. The prepared $Ni(OH)_2$/MWCNTs composite thin films were annealed at 573 K for 2 h to remove hydroxide content. The electrochemical surface reactivity of NiO is dependent on its crystallinity and annealing temperature. A number of reports indicate the utmost capacitance of NiO electrode materials was obtained by annealing at 573 K.[20−22] The films obtained at different layers of substrate immersion as 3:1, 1:1, and 1:3 are hereafter labeled as NC13, NC11, and NC31, respectively (N-NiO and C-MWCNT). The mass of active material for NC13, NC11, and NC31 samples are 0.27, 0.33, and 0.70 mg cm^{-2}, respectively. Finally, the prepared samples are employed for further characterizations.

Morphological and Compositional Analyses. The surface morphology of the NC nanocomposite hybrids is shown in Figure 1. As demonstrated in Figure 1a, b, d, and e, the NC13 and NC11 nanocomposite hybrids demonstrate, highly porous morphology composed of bunch-of-worms-type distribution of NiO nanospots and nanoparticles loaded on MWCNTs, respectively, robustly proposing the presence of a large amount of micropores in these materials. While the NC31 nanocomposite hybrid exhibits porous morphology constituting the dense nanoparticles incorporated with MWCNTs; see Figure 1g. At high magnification, it is seen that on these dense nanoparticles, porous morphology constituting the nanoflakes was grown (shown by yellow arrows in Figure 1g and h). Such dense, compact, and nanoflake-like morphology of NiO/MWCNTs is a consequence of nanoparticles growth, as a result of high cycle ratio of $Ni(OH)_2$ to MWCNTs, on the walls of MWCNTs. Such dense morphology may reduce the specific surface area, porosity, and conductivity of the composite. In contrast, the nanospots loaded MWCNTs sample (as a result of low cycle ratio of $Ni(OH)_2$ to MWCNTs) may offer high specific surface area and porosity,

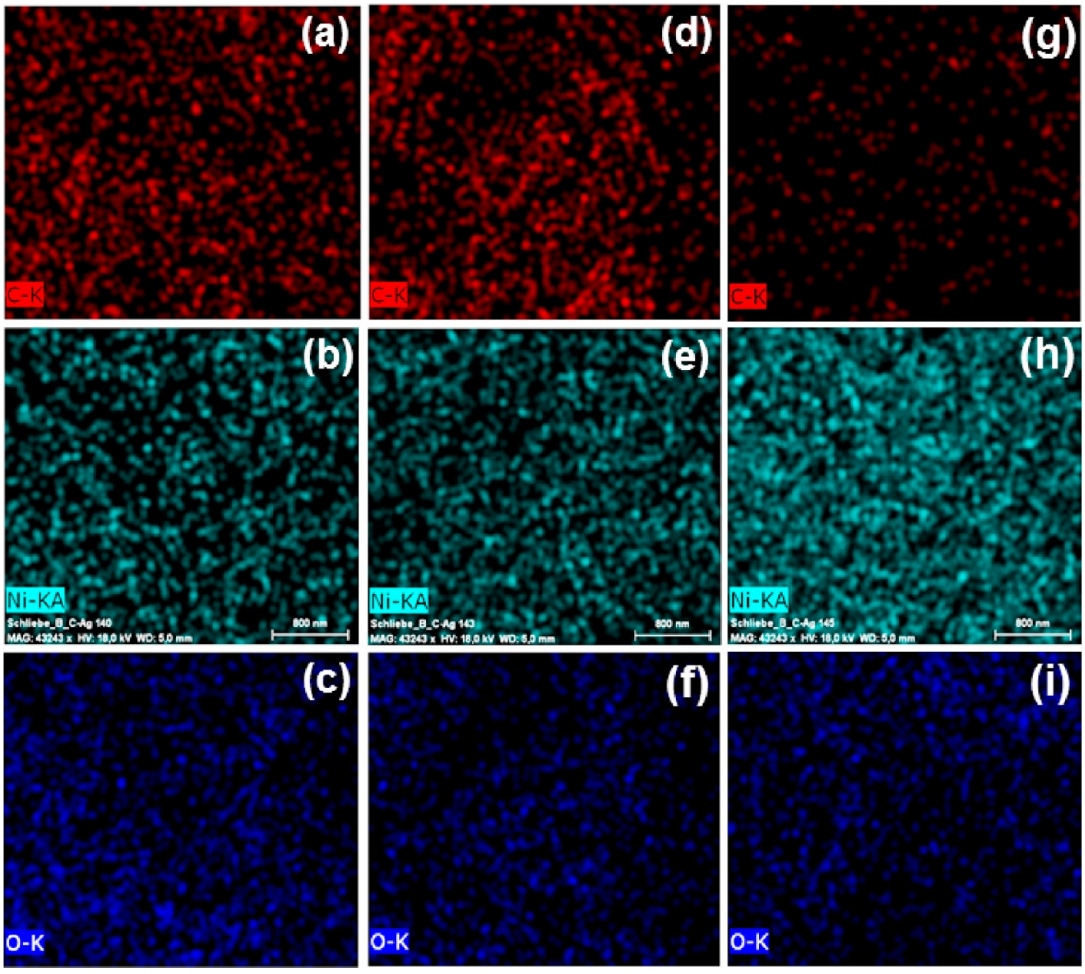

Figure 2. Elemental mapping/FE-SEM data of (a–c) NC13, (d–f) NC11, and (g–i) NC31 samples.

high conductivity to deliver the fast electrochemical kinetic process, and good chemical stability to NiO nanomaterials through $\pi-\pi$ interaction between walls of MWCNTs and NiO. This interaction is demonstrated schematically in Supporting Information Figure S1; the aromatic compounds on the surface of MWCNT stabilize metal oxide particles through $\pi-\pi$ interaction and offer more electrochemical stability for the metal oxide, similar the strategy described by Eder[23] for the composite of CdS, Fe_2O_3, TiO_2, Co, and Pt with CNT.

In addition, such a nanospot loaded MWCNTs composite will render as a 1D nanostructure, which maximizes the active materials utilization ratio and decreases the diffusion length significantly, resulting in high specific capacitance and excellent cycling stability. This examination reflects the sensibility and privilege of the SILAR method to assemble the nanostructures in forming the highly porous structure. The hybridization between NiO and MWCNT is additionally supported through EDS elemental mapping, presented in Figure 2. The entire carbon (C), nickel (Ni), and oxygen (O) elements are consistently dispersed in all portions of the NC nanocomposite hybrid thin film. Figure 2 clearly shows the nanometer-scale hybridization of all NC nanocomposite thin films. The EDS analysis spectra and atomic percentage in the NC nanocomposite hybrids are presented in Supporting Information Figure S2. This observation can help understand the contents of C, Ni, and O in three NC nanocomposite materials, where NC13: C and NC31: Ni/O is the expected content and proposes the suitability of SILAR method for the nanocomposite formation.

Furthermore, the shape and size of the NC nanocomposite hybrids are investigated and confirmed through TEM; see Figure 1c, f, and i. The TEM images of the nanohybrids distinctly illustrate the anchoring of nanospots and nanoparticles on MWCNTs for NC13 and NC11 samples, respectively, while dense nanoparticles incorporated with MWCNTs for the NC31 sample. The closest assessment of the TEM images demonstrates that the particle size of nanospots ranges from ~1 to ~3 nm, and that for nanoparticles ranges from ~5 to ~10 nm on the wall of MWCNTs. While densely packed nanoparticles integrated nanoflakes with MWCNTs, confirmed from Figure 1i, and exhibited thickness range from ~20 to ~35 nm by means of FE-SEM image in Figure 1h. This examination impressively proposes that the external surface of NC13 nanohybrid, nanospots decorated on the walls of MWCNTs, can render the highly porous structure and can strongly amplify the electrochemical performance. While nanoparticles coated MWCNTs and dense nanoparticle supported nanoflakes with MWCNTs may diminishe the porosity of NC11 and NC31 composites and consequently affect the electrochemical features.

Structural and Surface Area Analyses. The progress of the crystal structure of NC nanohybrids powder, scratched from NC composite thin films, was investigated with X-ray diffraction (XRD) analysis. The formation of hybrid and FCC

crystal structure is confirmed from XRD patterns (Figure 3). As projected in Figure 3, all NC nanohybrids exhibit principal

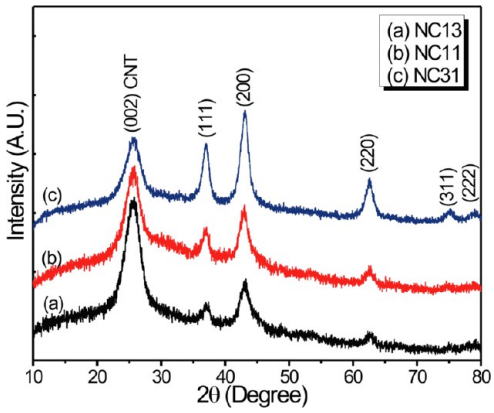

Figure 3. Powder XRD patterns of (a) NC13, (b) NC11, and (c) NC31 samples.

graphitic (002) peak of the MWCNTs at 25.55° and broad peaks along (111), (200), (220), (311), and (222) planes at 37.0°, 43.1°, 62.8°, 75.1°, and 78.8° reflections, matching well with the standard pattern (JCPDS-ICDD No. 895881) of FCC crystal structure. The absence of any minor peaks in the XRD patterns clearly illustrates the phase purity and complete decomposition of NC samples after annealing at 573 K. Additional effects observed in XRD patterns are as follows: (i) the peak becomes more broad from NC31 to NC13 samples, related to the nanocrystalline nature of NC13 sample; (ii) the intensity of the graphitic (002) peak diminishes and (200) peak (of NiO) amplifies (and narrows) from NC13 to NC31, possibly corresponding to more content of MWCNT and more crystallinity of NiO in NC13 and NC31 samples, respectively.

The formation of hybridization is additionally supported through the Raman spectra as shown in Figure 4, which includes peaks associated to Raman active vibrational modes of NiO and MWCNTs. Peaks at 516.9, 1359.4, 1587.8, and 2724.6 cm^{-1}, respectively, are related to Ni−O stretching mode, D, G, and 2D bands of graphitic carbon materials.[23−26] The sharp and strongest features of Raman peaks implicate the increment in grain size and concentration of contents in the material. The

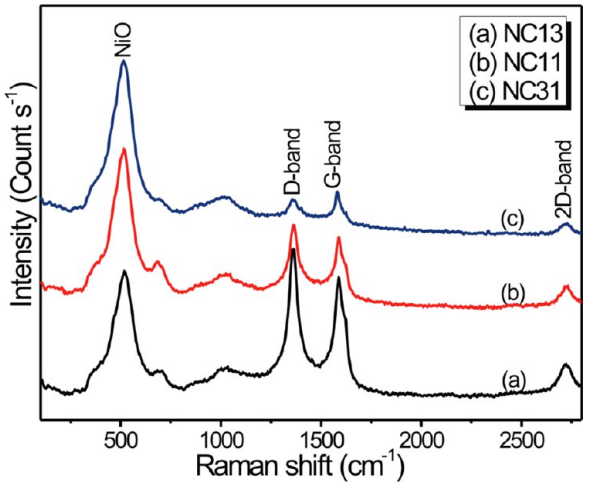

Figure 4. Raman spectra of (a) NC13, (b) NC11, and (c) NC31 samples.

sharpness of the Ni−O stretching peak for the NC31 sample and D, G, and 2D band peaks for NC13 samples may be related to more crystallinity of NiO and utmost content of MWCNT in the same samples, respectively. The nanocrystalline phase of NiO with decorated on MWCNTs in NC13 sample is advantageous for electrochemical capacitors, since it offers penetration path through the bulk material, and the entire electrode material can be employed for energy storage.

The porosity and surface area of the NC nanohybrids are probed through N_2 adsorption−desorption isotherm studies. Figure 5A clearly illustrates much larger amount of N_2 gas

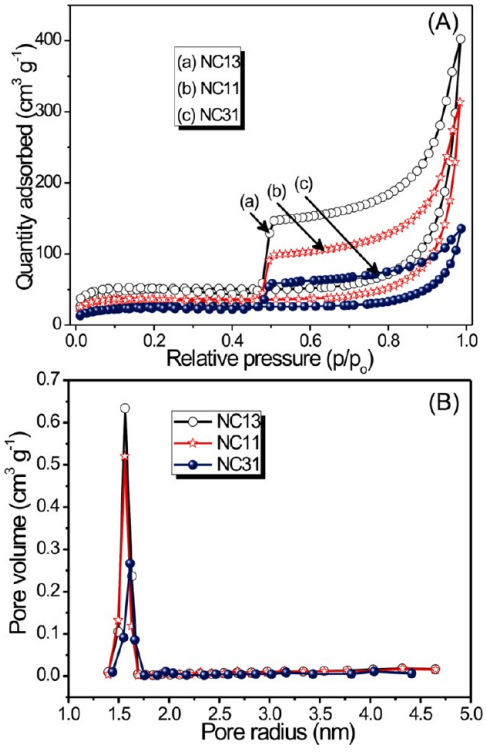

Figure 5. (A) Nitrogen adsorption−desorption isotherms and (B) pore size distribution curves of NC13, NC11, and NC31 samples.

adsorbed by NC13 samples than in the case of the NC31 hybrid, which robustly proposes the enhancement of surface area for NC13 sample. All of the nearby nanohybrids exhibit Brunauer−Deming−Deming−Teller (BDDT)-type IV shape of isotherms with a H3-type hysteresis loop in the IUPAC classification, manifesting the formation of micropores and mesopores.[27] Consequently, the significant adsorption of N_2 molecules emerges at a relatively low pressure region, demonstrating the coexistence of micropores and mesopores in nanohybrids. The fitting investigation based on the Brunauer−Emmett−Teller (BET) equation reveals the enlargement of surface area of the NC31 nanohybrid ∼74.22 to ∼128.16 m^2 g^{-1} for NC11, and ∼152.02 m^2 g^{-1} for NC13 nanohybrids. This determination establishes that nanospots of NiO decorating on MWCNTs through the SILAR cycle ratio of 3:1 for MWCNTs/$Ni(OH)_2$ constructs a potential tool for significant enhancement of the surface area of nanohybrids. The pore size distribution of the NC nanohybrids is analyzed through employing the Barrett−Joyner−Halenda (BJH) technique. From Figure 5B, it can be verified that all of the nanohybrids have micropores with the average radius of ∼1.4−1.7 nm. The very diminutive basal spacing of the nanohybrids

dx.doi.org/10.1021/am404422g | ACS Appl. Mater. Interfaces 2014, 6, 3176−3188

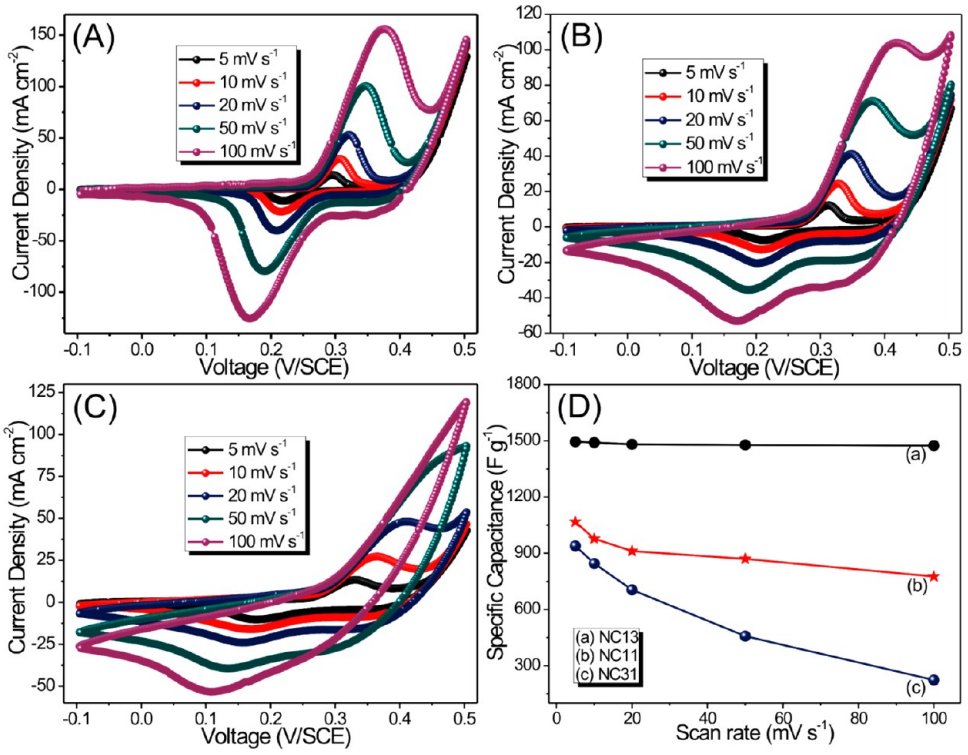

Figure 6. Cyclic voltammograms of (A) NC13, (B) NC11, and (C) NC31 samples at different scan rates. (D) Plots of specific capacitance versus potential scan rate for (a) NC13, (b) NC11, and (c) NC31 samples.

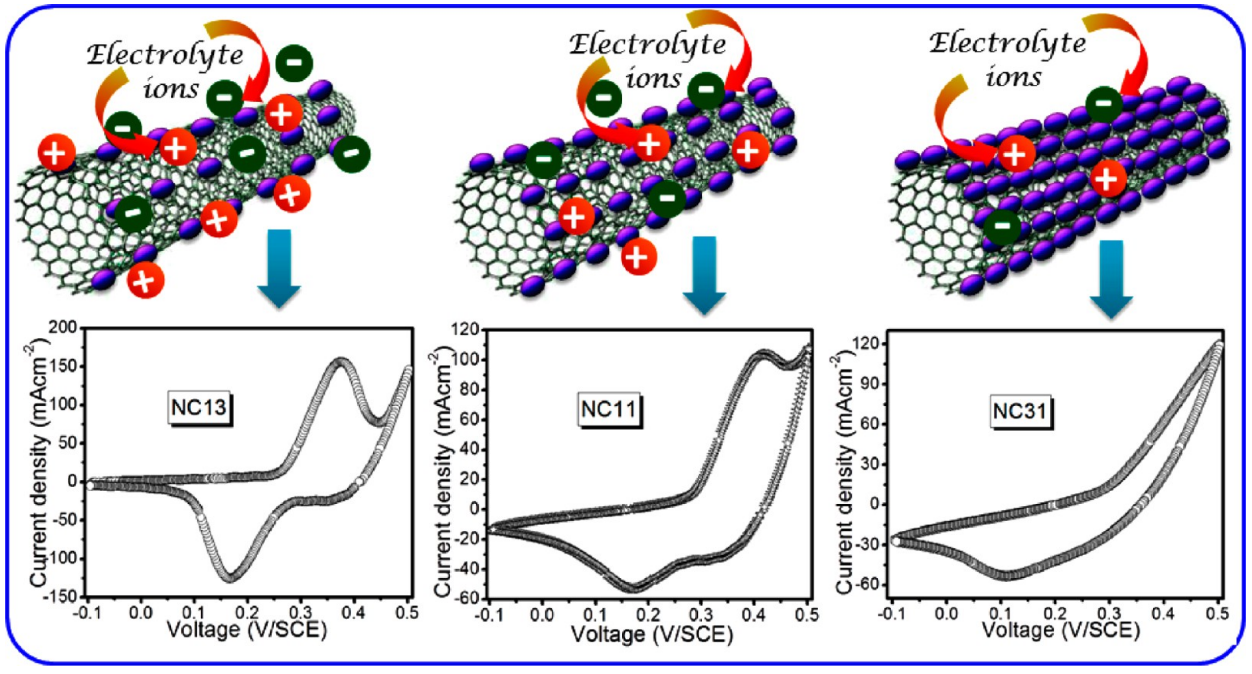

Figure 7. Schematic representation of impact of mass loading effect on the intercalation/deintercalation of ions and subsequently on CV curves.

than the diameters of micropores cleanly suggests the formation of micropores may be credited to micropore walls of MWCNTs and the interconnected structure of fine particles of NiO and walls of MWCNTs. Also as presented in Figure 4a and b, BET specific surface area, pore volume, and BJH pore size are increased with the increasing MWCNTs content. This is very supportive and essential to offer low-resistance pathways through the porous structure and to enhance charge storage, charge transport, and power capability.

Electrochemical Supercapacitive Properties. The cyclic voltammogram (CV) measurements were executed to examine impact of NiO nanostructures and mass loading on MWCNTs as an active material, since CV has ideal features for analyzing the capacitive performance such as large magnitude of current and a rectangular type of voltammogram, symmetricity in

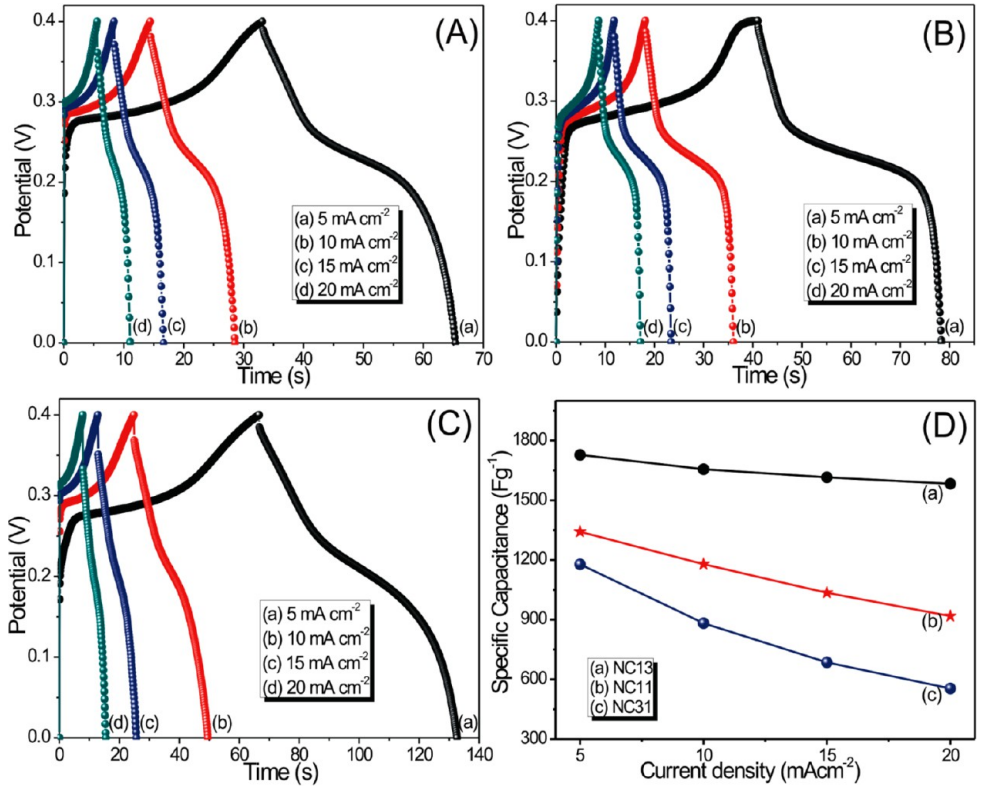

Figure 8. Galvanostatic discharge curves of (A) NC13, (B) NC11, and (C) NC31 samples at different current densities. (D) Variation of specific capacitance with discharging current density for (a) NC13, (b) NC11, and (c) NC31 samples.

anodic and cathodic directions, and so forth. As illustrated in Figure 6A–C, the cyclic voltammetry curves of NC13, NC11, and NC31 nanohybrids were measured in 2 M KOH electrolyte with a −0.1 to +0.5 V/SCE operational window at different scan rates. The responses of NC nanohybrids were very close to ideal pseudocapacitive behavior without showing any polarization, as every CV curve of NC nanohybrids comprises a strong redox peak excluding a regular rectangular shape as a result of electric double layer capacitance. In addition, other pseudocapacitive features exhibited by the NC hybrids are (i) reversibility represented by the two noticeable peaks, (ii) different shapes of CV curves for different NC hybrids, as a consequence of different nanostructures, and (iii) the potential of the anodic and cathodic peak shifts in the more positive and negative directions, as the scan rate is increased. The redox mechanism may be the result of NiO/NiOOH redox pair, which can be explained via following electrochemical reaction:

$$x\mathrm{NiO} + z\mathrm{OH}^- \rightarrow z\mathrm{NiOOH} + (x - z)\mathrm{NiO} + ze^- \qquad (4)$$

The obtained values of specific capacitance for three NC nanohybrids are plotted with respect to scan rate, as presented in Figure 6D. According to eq 5, the specific capacitance is proportional to the current and inversely proportional to the scan rate and mass loading of the electrode. In addition, the intercalation of ions from the solution to the active material during charging significantly depends upon its microstructure, specific surface area, and porosity. The nanostructure materials with high specific surface area and microporous structure encourage utilization of electrode material and demand enough time for charging and same for deintercalation during discharging, which results in advanced specific capacitance called ion exchange mechanism.[28−30]

The nanoparticles decorated MWCNTs (NC11) and nanoflakes incorporated with MWCNTs nanohybrids (NC31) demonstrate less specific capacitance and decrement of specific capacitance with the scan rate, while nanospots printed on MWCNTs (NC13) nanohybrid exhibits maximum specific capacitance (1495 F g^{-1}) with very negligible loss of specific capacitance (1495−1475 F g^{-1}) with the scan rate and significantly support the ion-exchange mechanism. All these consequences of ion transport, within the different nanostructured and mass loaded NiO/MWCNTs nanohybrids, are schematically portrayed in Figure 7. Subsequently, the value of ΔV_p ($V_{po} - V_{pr}$) is necessary in evaluating the reversibility of the redox reaction, where ΔV_p is the potential difference between the two peaks (oxidation and reduction), V_{po} is the potential of the oxidation peak, and V_{pr} is the potential of reduction peak. The lowest value of ΔV_p suggests the greatest reversibility of the supercapacitor electrode, which is clearly attributed to the NC13 nanohybrid. In addition, the comparative capacitive performance of MWCNT, NiO, and NC composite thin films, along with their surface morphology and X-ray diffraction measurements and improved capacitance for NC13 composite as compared to two other composites, MWCNT and NiO thin films, are provided in Supporting Information Figure S3.

Furthermore, the galvanostatic charge/discharge (GCD) measurement is a better gauge of supercapacitive performance for probing the redox reaction and monitoring the pseudocapacitive nature of the electrodes materials. Additionally, this technique is offered to judge the rate of change of voltage with time during both charging and discharging at different current densities and a stable potential window. Therefore, this technique is also advantageous to evaluate the

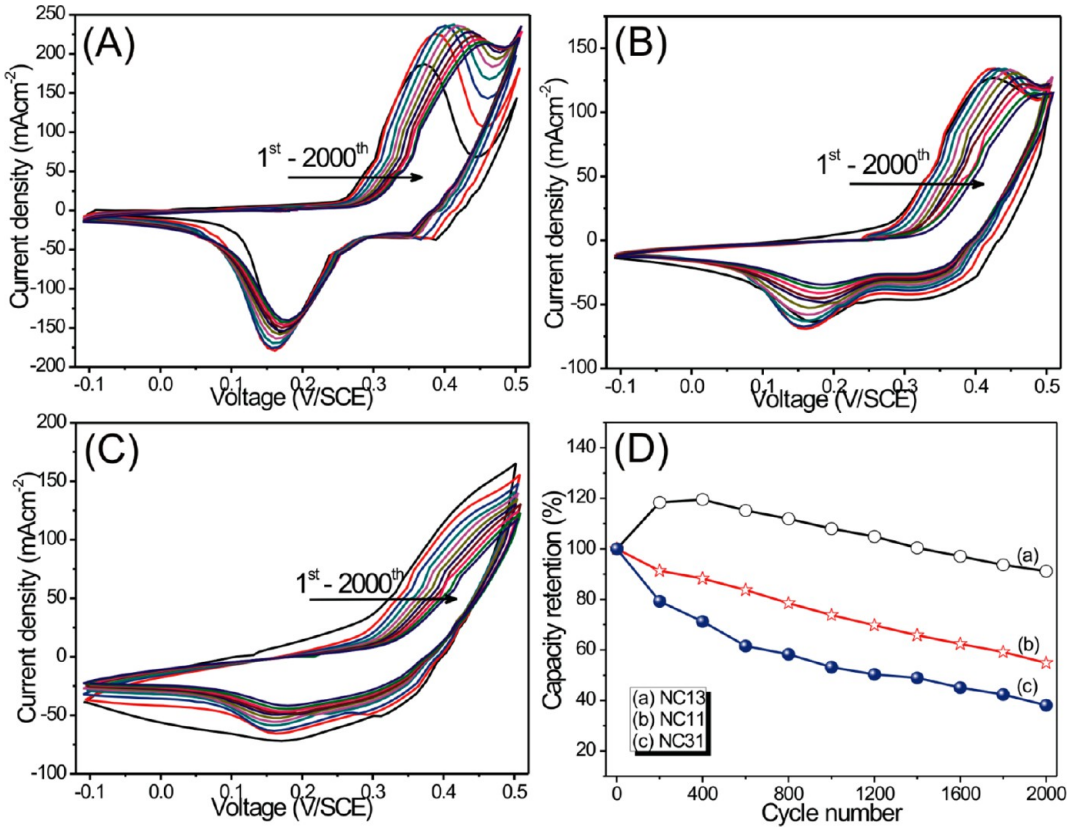

Figure 9. CV curves of (A) NC13, (B) NC11, and (C) NC31 samples for different CV cycles. (D) Plots of capacitive retention with the number of cycles for (a) NC13, (b) NC11, and (c) NC31 samples.

rate capability of the electrode material. The charge/discharge curves of the NC13, NC11, and NC31 nanohybrid samples in 2 M aqueous KOH electrolyte at different current densities are plotted, as a potential−time profile, in Figure 8A−C. The nonlinear line profiles of all samples support the pseudocapacitive nature of the electrodes, since a double layer capacitor preferably yields a triangular-wave-like profile for a charge/discharge cycle. The discharging curve shows three different regions: (i) the initial drop in the voltage is related to the internal resistance of the electrode material; (ii) the linear variation of potential with time corresponds to double layer capacitance owing to the charge separation at electrode/electrolyte interface; and last (iii) the deviation of slope of potential versus time profile discloses the redox reaction between electrolyte and NC nanohybrid electrodes.[31]

The evaluated values of specific capacitance for different nanohybrids at different current densities of 5, 10, and 20 mA cm^{-2} are plotted in Figure 8D. The maximum specific capacitance (1727 F g^{-1}) of NC13 nanohybrid is a consequence of its high specific surface area and microporous structure. Furthermore, the nanospots (of NiO) loaded MWCNTs nanohybrid (NC13) has larger pore volume which absorbs more water molecules, facilitates a buffering reservoir to accommodate ions for the redox reaction, provides conducting pathways through facilitating maximized contact and fast diffusion, and leads to improvement in kinetics of the reversible redox process for charge storage through diminishing internal resistance (IR) drop,[32,33] as clearly demonstrated in Figure 8A−C. The decrement of specific capacitance for other nanohybrids (NC11 and NC31) is credited to comparatively low specific surface area and small pore radius, and significantly supports the ion-exchange mechanism. Moreover, the enhanced electrode material utilization of NC13 nanohybrid is clearly reflected in Figure 8D. The small variation in specific capacitance is clearly observed for all the samples evaluated through GCD and CV measurements. The reason behind the divergence in the specific capacitance for GCD and CV measurements is that the value of specific capacitance estimated through CV measurement is at a particular potential, while GCD measurement offers an average capacitance over the potential range of 0−0.4 V. These averaging capacitances in a voltage range may cause variation in the specific capacitance.[34,35]

The effect of NC hybridization on the electrochemical stability is evaluated through monitoring 2000 potential cycling in 2 M KOH electrolyte at a scan rate of 100 mV s^{-1}, since the long-term cycling stability of the electrode is the most important parameter used for measuring characteristics of a supercapacitor. Furthermore, the plots of CV curves versus number of CV cycles for different nanohybrids are shown in Figure 9A−C. Moreover, the plot of capacitive retention with the cycle number for different NC nanohybrids is demonstrated in Figure 9D. Among all the NC nanohybrids, the NC13 nanohybrids show 20% enhanced capacitive performance up to 400 cycles, which may be a consequence of integration voltammetric charges from the positive and negative sweeps of the CVs, and came closer to each other in magnitude with increasing cycle number. In addition, NC13 nanohybrid capacitance is decreased by 9% of the maximum specific capacitance. Since the walls of MWCNTs in NiO/MWCNTs nanohybrid offer good chemical stability to NiO nanomaterials through $\pi-\pi$ bonding with the side wall of MWCNTs, this

Table 1. Comparative Representation of Different Aspects of NiO/CNTs Composite for Supercapacitor Application

material	method	substrate	specific capacitance (F g^{-1})	capacitive retention (%)/stability	ref
NiO/CNTs	hydrothermal (powder method)	nickel grid	1329	~93/1000	38
NiO/CNTs	electrochemical precipitation	CNT paper	1000		39
NiO/CNTs	reflux precipitation (powder method)	nickel foam	328	64.3/300	12
NiO/CNTs	chemical precipitation (powder method)	nickel foam	165	100/100	40
NiO/MWCNTs	SILAR	stainless steel	1727	91/2000	present work

bonding promotes to stabilize NC nanohybrid mechanically and avoid the loss of electrode material in the cycling test besides the general trend of dissolution of NiO into electrolyte solution.[36] However, the capacitive retention is dramatically diminished for NC11 (55%) and NC31 (38%) nanohybrids. This may be due to increased mass loading cause to $\pi-\pi$ bonding of NiO nanomaterials with walls of MWCNTs, which results into more dissolution of electrode material into the electrolyte solution. In addition, nanospots loaded MWCNTs nanohybrid (NC13) offers a 1D network, leads to the slow dissolution of electrode material, which may enhance the surface area electrode, and offers more electrochemical active sites. Whereas NC11 and NC31 nanohybrids provide 3D network causing fast dissolution of electrode material.[37]

Formerly, charge−discharge profiles of NiO/CNT composite were examined by many investigators to obtain superior electrochemical properties of NiO. All the details of literature survey on NiO/CNTs composite are summarized in Table 1. The values of electrochemical parameters reported in the present study are superior to those obtained earlier for NiO/MWCNT composite electrodes. The present NC nanohybrids electrodes are too cost-effective, since electrodes employed are stainless steel substrates. In addition, the enhanced outcomes in the present study may be consequences of (i) the advantages of the SILAR method such as preparation through binder-free, additiveless approach to avoid dead free surface and low temperature method of preparation, (ii) the enhancement of electrode material conductivity and nanostructure through fine control of SILAR cycle ratio, and (iii) actually, in all of the above reports, NiO nanoparticles are only mixed with MWCNTs that are not uniformly attached to the walls of MWCNTs.

The Ragone plot (power density vs energy density) of the NC nanohybrids, which constitutes the operational performance/efficiency of different nanostructures as a supercapacitor electrode, is illustrated in Figure 10A. All the nanohybrids exhibit high power density relative to conventional batteries and maintain high energy density as inflected by conventional capacitors. The increasing fashion of the power and energy density from NC31 to NC11 nanohybrid may be credited to higher conductivity of electrode material and higher content of MWCNTs. Subsequently, these results evidently demonstrate the superiority of the SILAR method for controlling the rate capability of electrode material.

The electrochemical impedance spectroscopy (EIS) analyses were performed to examine charge transfer rate of electrolyte ions through the different nanohybrids. The Nyquist plot of NC nanohybrids in the frequency range 100 kHz to 100 mHz is illustrated in the Figure 10B. All impedance spectra have a semicircular arc and straight line. The *X*-intercept of the Nyquist plots relates to the equivalent series resistance (R_s), which includes the contributions of electronic and ionic resistances.[41,42] The intrinsic resistance of the material corresponds to electronic resistance, while the interfacial

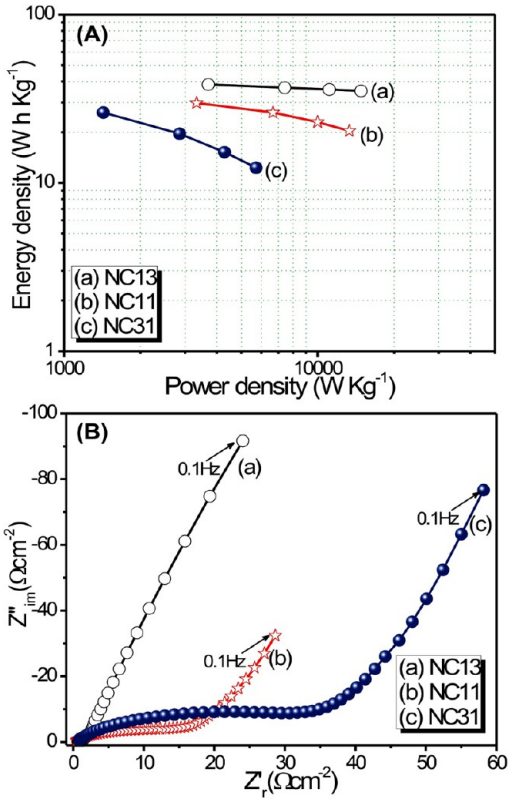

Figure 10. (A) Ragone plots as specific power versus specific energy and (B) Nyquist plots of (a) NC13, (b) NC11, and (c) NC31, samples.

resistance is an integration of interparticles resistance and resistance among particles and current collector. The ionic (diffusion) resistance of ions through pores and the electrolyte resistances in the pores are coupled to ionic resistance. The semicircle arc in the high-frequency region is a result of the charge transfer resistance (R_{ct}), which is a related to the faradaic reactions and the double layer capacitance (C_{dl}) at the electrode/electrolyte interface.[43,44] R_{ct} can be calculated from the diameter of semicircular arc. The measured values of R_s and R_{ct} for different nanohybrids are summarized in Table 2. The summarized values of R_s and R_{ct} for NC13 nanohybrids are smaller than those of the other two nanohybrids (NC11 and

Table 2. Electrochemical Parameters of NiO/MWCNTs Composite Samples Estimated through EIS Study

	parameters	
samples	*Rs* (Ω cm^{-2})	R_{ct} (Ω cm^{-2})
NC13	0.54	1.72
NC11	0.65	12.02
NC31	0.79	37.38

dx.doi.org/10.1021/am404422g | ACS Appl. Mater. Interfaces 2014, 6, 3176−3188

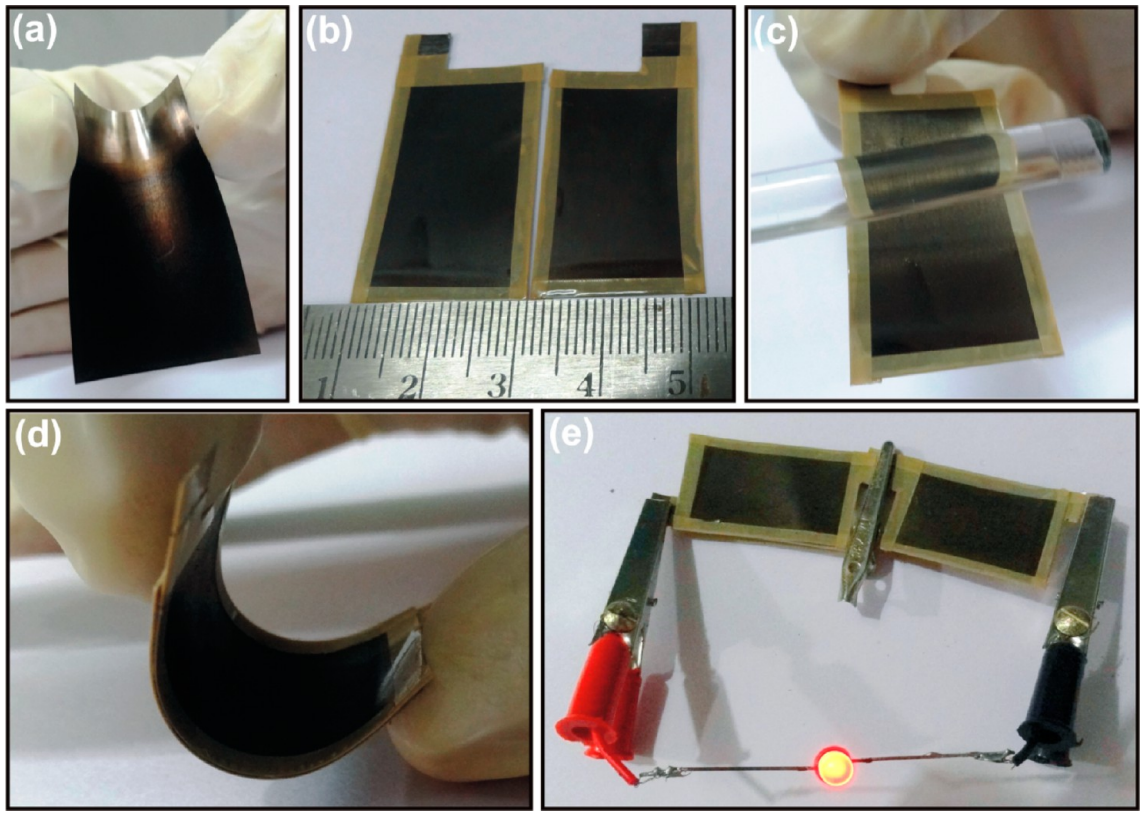

Figure 11. Fabrication of highly flexible NiO/MWCNTs-NiO/MWCNTs nanohybrid symmetric device: (a) digital photograph of flexible NiO/MWCNTs nanohybrid thin film on the stainless steel substrate, (b) NiO/MWCNTs nanohybrid electrodes (2×3 cm^2 area) with sealed edges, (c) PVA/$LiClO_4$ gel electrolyte coating on the electrode, and (d) flexible supercapacitor constructed through sandwiching the two gel electrolyte coated electrodes under the ~1 ton pressure. (e) The two flexible supercapacitor in series can be effectively employed to power a LED.

NC31) and strongly support the CV, GCD, and electrochemical stability measurements.

Fabrication, Demonstration, and Performance Evaluation of Symmetric (NC13/NC13) Solid State Supercapacitor. In order to ensure commercialization of SILAR deposited NC13 nanohybrid electrode, it was scaled on a large area (2×3 cm^2) flexible stainless steel substrate, as shown in Figure 11a. So as to fabricate symmetric device, the edges of electrodes are sealed with adhesive tape to avoid any short; see Figure 11b. Furthermore, PVA/$LiClO_4$ gel electrolyte was painted on the NC13 nanohybrid electrode (shown in Figure 11c) and two electrodes were sandwiched in order to assemble the supercapacitor. In addition, the pressure ~1 ton is applied on the assembled supercapacitor, with the intention of good contact and to improve its mechanical properties, as shown in Figure 11d. When the two devices in series were charged fully, they could power a commercial LED (Figure 11e).

The digital photographs of a flexible-solid-state supercapacitor device at different bending angles (manually) are demonstrated in Figure 12A−C, in order to show the mechanical flexibility of the device. The cyclic voltammograms of the flexible-solid-state symmetric (NC13/NC13) supercapacitor within the potential window of −0.6 to +0.6 V at different scan rates (from 5 to 100 mV s^{-1}), are demonstrated in Figure 12D. The ideal features of electrode materials, such as larger loop area of the CV curves, rectangular type of voltammogram, and symmetric in anodic and cathodic directions, are clearly reflected from the CV curves (Figure 12D). The estimated values of specific capacitance are decreased from 24 to 13 F g^{-1} with increasing scan rate (5−100 mV s^{-1}). Furthermore, the mechanical flexibility of the devices is a significant factor during construction of supercapacitors for portable electronic applications. In order to evaluate the performance of the devices at the bent stage, we carried out CV measurement at 50 mV s^{-1} scan rate (Figure 12E), during which the device was bent at 0°, 45°, 90°, and 135°. The good capacitive retention is observed for the test at all bending angles, as illustrated in Figure 12F. The bending test was performed sequentially, and the angles were changed manually, as demonstrated in Figure 12A−C. The good cycling stability is a necessity for the commercialization of the device. Therefore, the cyclic stability of the flexible-solid-state symmetric supercapacitor device was executed using CV measurements for 2000 cycles at scan rate of 100 mV s^{-1}. Figure 12G represents the CV curves of the device at different cycle numbers. The estimated capacitive retention for the device after 2000 CV cycles is 50%. To the best of our knowledge, NiO/MWCNTs based flexible-solid-state supercapacitor device on cost-effective stainless substrate has not been systematically and quantitatively measured and demonstrated.

CONCLUSIONS

The used SILAR method offers additive-free and binderless route to avoid dead surface in the traditional powder method, with very fine controlled tool to modify composite morphology, mass loading of metal oxide on MWCNTs, and eco-friendly and cost-effective path for large area deposition. The NiO nanospots loaded MWCNTs nanohybrid yields microporous structure with enhanced electrochemical supercapacitive

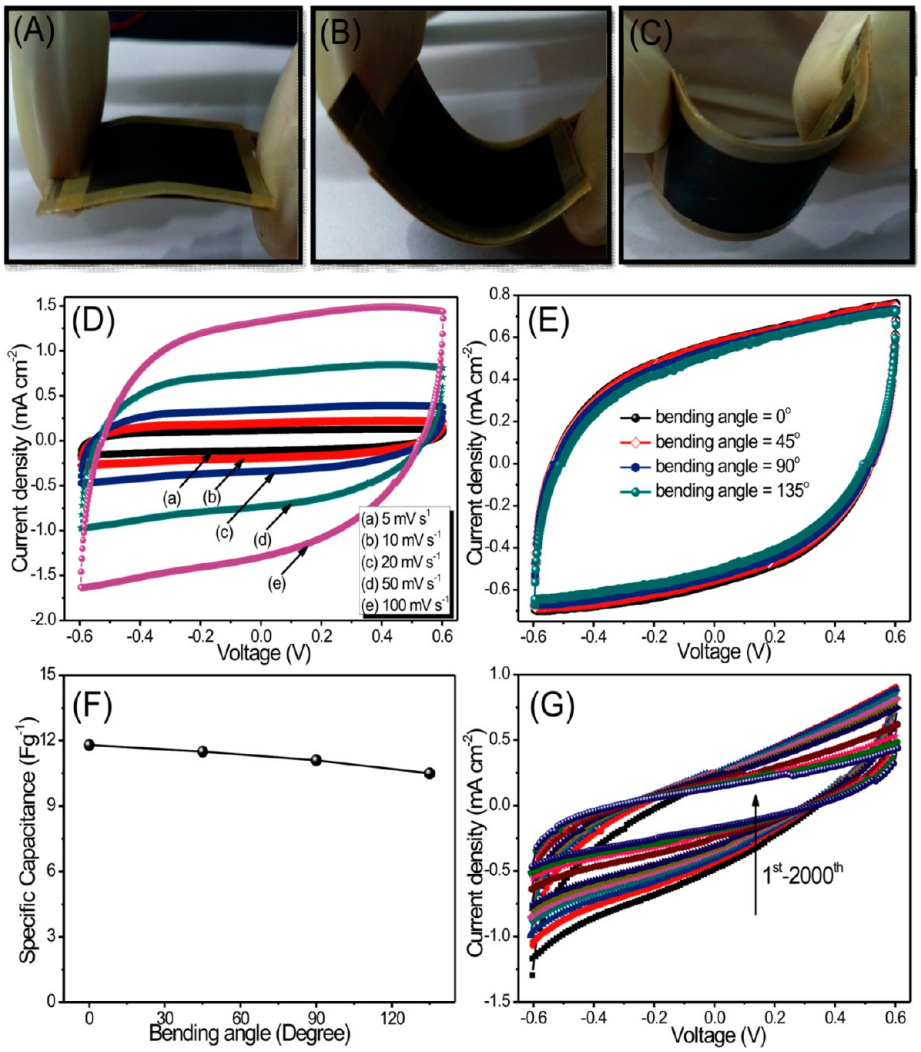

Figure 12. (A–C) Digital photographs of the flexible-solid-state device at different bent angles. (D) CV curves of flexible-solid-state symmetric supercapacitor device at different scan rates. (E) Cyclic voltammograms of symmetric devices at different bent angles. (F) Variation of specific capacitance of devices at different bent angles. (G) CV curves of flexible-solid-state symmetric supercapacitor device for different cycle numbers (from 1st to 2000th) at the scan rate of 100 mVs^{-1}.

properties such as utilization of electrode material, reversibility, specific capacitance, electrochemical stability, fast charge–discharge rate, power density, and charge transfer resistances. Furthermore, a highly flexible solid supercapacitor built from NiO nanospots loaded MWCNTs (NC13) nanohybrid offers the successful usage to fire commercial LED and good electrochemical performance even at different bending angles. This suggests that NC13 nanohybrid is a promising electrode material for future energy storage systems.

EXPERIMENTAL SECTION

Synthesis of NiO/MWCNT Nanocomposite. In the present work, NiO/MWCNT thin films have been fabricated onto the flexible stainless steel (FSS) substrate through the alternate immersion of substrates in alkaline metal salt bath (source of Ni^{2+} ions) at room temperature and diluted (2%) H_2O_2 solution maintained at 333 K (source of OH^- ions). A three-beaker SILAR system was employed to prepare the NiO/MWCNT thin film onto FSS substrates. In brief, functionalized MWCNTs of 0.01 mg were sonicated in 50 mL of double distilled water for several hours to form steady and uniform dispersions. This dispersed MWCNTs solution is used as the first beaker. Functionalization of MWCNTs was performed via the acid treatment.[45] Aqueous nickel sulfate (0.05 M) solution (second beaker) was used as a source of Ni ions, which was made alkaline by addition of aqueous ammonia solution to compose the pH of solution pH ~ 12. Lastly, the third beaker acts as a source of hydroxyl ions, which includes deionized water with a few drops of H_2O_2 (1%) solution maintained at 333K. Initially, the ultrasonically treated and well-cleaned SS substrates were immersed in the MWCNT solution for 30 s, during the time MWCNTs were adsorbed onto the substrate surface. Further, the substrate was dipped in an alkaline nickel sulfate solution for 30 s to adsorb the nickel complex ions onto the surface of the preadsorbed MWCNTs. After immersion of the substrate into the H_2O_2 solution for 30 s, maintained at 333 K, a reaction took place at the MWCNT surfaces to form $Ni(OH)_2$ nanoparticles (so, the last two beakers accord to form $Ni(OH)_2$). This cycle was repeated several times (80) to increase the thickness of the $Ni(OH)_2$/MWCNT thin film. The representation of SILAR method for deposition of $Ni(OH)_2$/MWCNTs is shown in Supporting Information Figure S4. The as-deposited films were annealed at 573 K to remove the hydroxide phase and to form the NiO/MWCNTs composite. In order to carry out the mass loading of active material (NiO on MWCNT), the single cycle was composed of different layers of MWCNT and $Ni(OH)_2$ as 3:1, 1:1, and 1:3. The cycle of different layers was repeated 80 times to achieve the terminal thickness for NC31 film and kept constant for two other samples, that is, NC13 and NC11, with the

dx.doi.org/10.1021/am404422g | ACS Appl. Mater. Interfaces 2014, 6, 3176–3188

intention to examine the influence of mass loading on electrochemical performance.

Materials Characterization. The morphologies of the resulting samples were visualized by field-emission scanning electron microscopy (FE-SEM, JEOL JSM 6390) attached with an energy-dispersive X-ray spectroscopy (EDS) analyzer to measure the sample composition. The transmission electron micrographs were visualized using a JEOL JEM-2100 instrument operated at 200 kV. Powder X-ray diffraction (XRD) experiments (Bruker axs D8, λ = 1.54 A°) were performed to examine the crystal structure of the NC13, NC11, and NC31 nanocomposite powders peeled from thin films. Micro-Raman spectra were measured, using a Jobin Yvon Horibra LABRAM-HR visible spectrometer with an argon-ion continuous-wave laser (488 nm) as the excitation source, to confirm the composite formation and phase of NiO in the present hybrids. The volumetric N_2 adsorption/desorption studies were carried out, to examine surface area and pore structure of the present nanocomposite hybrids, by Brunauer–Emmett–Teller (BET) measurement using an ASAP-2010 surface area analyzer. The mass of the electroactive materials on the film was estimated through the weight difference method using the sensitive microbalance.

Evaluation of Electrochemical Measurements. Cyclic voltammograms (CVs), galvanostatic charge–discharge (GCD), and electrochemical impedance studies were carried out, to evaluate the electrochemical properties of the NiO/MWCNTs (NC) composite thin films, using the electrochemical workstation (ZIVE SP5). The electrochemical impendence measurements were assessed in the frequency range of 100 kHz to 100 mHz with the AC amplitude of 10 mV. An electrochemical cell composed of NC thin films as a working electrode, platinum as a counter electrode and saturated calomel electrode (SCE) as a reference electrode. The specific capacitances of NC nanohybrids were calculated from the cyclic voltammetry study using the following equation:

$$C = \frac{1}{m\nu(V_c - V_a)} \int_{V_a}^{V_c} I(V)\, dV \tag{5}$$

where C is the specific capacitance (F g^{-1}), ν is the potential scan rate (mVs^{-1}), $V_c - V_a$ is the potential window, $I(V)$ denotes the response current (mA), and m is the deposited mass of the NC nanohybrid material on electrode for unit area (here 1 cm^2) dipped in electrolyte, which is estimated through the following relation:

$$m = m_2 - m_1 \tag{6}$$

where m_2 is mass of the substrate with film and m_1 is mass of the substrate without film. The specific capacitances (C_s) of NC nanohybrid electrodes have been evaluated from the potential–time profile at different current densities using the following equation:

$$C_s = \frac{I_d T_d}{\Delta V m} \tag{7}$$

where I_d (mA) is the constant discharge current density (mA cm^{-2}), T_d (s) is the discharge time, and ΔV (V) is the potential window.

The energy density (E, W h kg^{-1}) and power density (P, W kg^{-1}) of different nanohybrid samples were evaluated using the following equations:[46]

$$E = \frac{0.5 C_s (V_{max}^{\ 2} - V_{min}^{\ 2})}{3.6} \tag{8}$$

$$P = \frac{E3600}{T_d} \tag{9}$$

where V_{max} and V_{min} are the maximum and minimum potentials achieved during charging and discharging process, respectively, and are used in order to evaluate the effective energy and power densities which may be affected by used voltage difference.

■ ASSOCIATED CONTENT

Supporting Information

Schematic of functionalization, adsorption of CNTs on SS surface substrate, adsorption of $Ni(OH)_2$ on CNT, and π–π interaction of NiO and CNT. EDS patterns and table of elemental atomic percentage of different samples, comparative study of surface morphology, XRD patterns, and electrochemical performance of MWCNT, NiO, and NC composite. Schematic representation of deposition of $Ni(OH)_2$/MWCNTs composite electrode through the SILAR method. This material is available free of charge via the Internet at http://pubs.acs.org.

■ AUTHOR INFORMATION

Corresponding Author

*Tel.: +91 231 2609225. Fax: +91 231 2609233. E-mail: l_chandrakant@yahoo.com.

Notes

The authors declare no competing financial interest.

■ ACKNOWLEDGMENTS

One of the authors (G.S.G.) is thankful to DAE-BRNS, BARC Mumbai, India for the award of, "JRF". Authors are also grateful to Department of Science and Technology (DST) for financial support through PURSE and FIST & University Grant Commission (UGC) India through DSA-I scheme. Authors are also thankful to UGC-DAE CSR, Indore centre for providing Raman facility.

■ REFERENCES

(1) Chu, S.; Majumdar, A. *Nature* **2012**, *488*, 294–303.
(2) Chen, Y.; Zhang, X.; Zhang, D.; Yu, P.; Ma, Y. *Carbon* **2011**, *49*, 573–580.
(3) Hu, C. C.; Chen, W. C.; Chang, K. H. *J. Electrochem. Soc.* **2004**, *151*, A281–A290.
(4) Xu, M. W.; Bao, S. J.; Li, H. L. *J. Solid State Electrochem.* **2007**, *11*, 372–377.
(5) Wang, H. L.; Casalongue, H. S.; Liang, Y. Y.; Dai, H. J. *J. Am. Chem. Soc.* **2010**, *132*, 7472–7477.
(6) Wang, X.; Wang, Y.; Zhao, C.; Zhao, Y.; Yan, B.; Zheng, W. *New J. Chem.* **2012**, *36*, 1902–1906.
(7) Hu, C. C.; Chen, J. C.; Chang, K. H. *J. Power Sources* **2013**, *221*, 128–133.
(8) Anantram, M. P.; Leonard, F. *Rep. Prog. Phys.* **2006**, *69*, 507–561.
(9) Lin, D.; Xing, B. *Environ. Sci. Technol.* **2008**, *42*, 7254–7259.
(10) Yuan, G.; Jiang, Z.; Aramata, A.; Gao, Y. *Carbon* **2005**, *43*, 2913–2917.
(11) Lee, J. Y.; Liang, K.; An, K. H.; Lee, Y. H. *Synth. Met.* **2005**, *150*, 153–157.
(12) Su, A. D.; Zhang, X.; Rinaldi, A.; Nguyen, S. T.; Liu, H.; Lei, Z.; Lu, L.; Duong, H. M. *Chem. Phys. Lett.* **2013**, *56*, 68–73.
(13) Lin, P.; She, Q.; Hong, B.; Liu, X.; Shi, Y.; Shi, Z.; Zheng, M.; Dong, Q. *J. Electrochem. Soc.* **2010**, *157*, A818–A823.
(14) Salunkhe, R. R.; Jang, K.; Lee, S.; Yu, S.; Ahn, H. *J. Mater. Chem.* **2012**, *22*, 21630–21635.
(15) Dubal, D. P.; Gund, G. S.; Lokhande, C. D.; Holze, R. *ACS Appl. Mater. Interfaces* **2013**, *5*, 2446–2454.
(16) Zhao, D.; Yang, Z.; Zhang, L.; Feng, X.; Zhang, Y. *Electrochem. Solid-State Lett.* **2011**, *14*, A93–A96.
(17) Hodes, G. *Chemical solution deposition of semiconductor films.* Marcel Dekker Inc.: New York, 2002.
(18) Lee, S. W.; Kim, B. S.; Chen, S.; Yang, S. H.; Hammond, P. T. *J. Am. Chem. Soc.* **2009**, *131*, 671–679.
(19) Wilkinson, G., Ed. *Comprehensive coordination chemistry.* Pergamon Press: Oxford, 1987; p 5.

(20) Nam, K.; Yoon, W.; Kim, K. *Electrochim. Acta* **2002**, *47*, 3201−3209.
(21) Wu, M.; Gao, J.; Zhang, S.; Chen, A. *J. Porous Mater.* **2006**, *13*, 407−425.
(22) Nam, K.; Kim, K. *J. Electrochem. Soc.* **2002**, *149*, A346−A354.
(23) Eder, D. *Chem. Rev.* **2010**, *110*, 1348−1385.
(24) Lee, S. H.; Cheong, H. M.; Park, N. G.; Tracy, C. E.; Mascarenhas, A.; Benson, D. K.; Deb, S. K. *Solid State Ionics* **2001**, *140*, 135−139.
(25) Dharmaraj, N.; Prabu, P.; Nagarajan, S.; Kim, C. H.; Park, J. H.; Kim, H. Y. *Mater. Sci. Eng., B* **2006**, *128*, 111−114.
(26) Kong, M.; Fei, J.; Wang, S.; Lu, W.; Zheng, X. *Bioresour. Technol.* **2011**, *102*, 2004−2008.
(27) IUPAC. *Pure Appl. Chem.* **1994**, *66*, 1739−1758.
(28) Pang, H.; Ma, Y.; Li, G.; Chen, J.; Zhang, J.; Zheng, H.; Du, W. *Dalton Trans.* **2012**, *41*, 13284−13291.
(29) Dubal, D. P.; Lee, S. H.; Kim, J. G.; Kim, W. B.; Lokhande, C. D. *J. Mater. Chem.* **2012**, *22*, 3044−3052.
(30) Dubal, D. P.; Gund, G. S.; Holze, R.; Lokhande, C. D. *J. Power Sources* **2013**, *242*, 687−698.
(31) Sugimoto, W.; Iwata, H.; Yasunaga, Y.; Murakami, Y.; Takasu, Y. *Angew. Chem., Int. Ed.* **2003**, *42*, 4092−4206.
(32) Kim, S.; Lee, J.; Ahn, H.; Song, H.; Jang, J. *ACS Appl. Mater. Interfaces* **2013**, *5*, 1596−1603.
(33) Foelske, A.; Barbieri, O.; Hahn, M.; Kotz, R. *Electrochem. Solid. St.* **2006**, *9*, A268−A272.
(34) Kelly, T. L.; Yano, K.; Wolf, M. O. *ACS Appl. Mater. Interfaces* **2009**, *1*, 2536−2543.
(35) Saravanakumar, B.; Purushothaman, K. K.; Muralidharan, G. *ACS Appl. Mater. Interfaces* **2012**, *4*, 4484−4490.
(36) Yu, G.; Hu, L.; Liu, N.; Wang, H.; Vosgueritchian, M.; Yang, Y.; Cui, Y.; Bao, Z. *Nano Lett.* **2011**, *11*, 4438−4442.
(37) Gund, G. S.; Dubal, D. P.; Jambure, S. B.; Shinde, S. S.; Lokhande, C. D. *J. Mater. Chem. A* **2013**, *1*, 4793−4803.
(38) Lin, P.; She, Q.; Hong, B.; Liu, X.; Shi, Y.; Shi, Z.; Zheng, M.; Dong, Q. *J. Electrochem. Soc.* **2010**, *157*, A818−A823.
(39) Nam, K. W.; Lee, E. S.; Kim, J. H.; Lee, Y. H.; Kim, K. B. *J. Electrochem. Soc.* **2005**, *152*, A2123−A2129.
(40) Lee, J. Y.; Liang, K.; An, K. H.; Lee, Y. H. *Synth. Met.* **2005**, *150*, 153−157.
(41) Wen, Z. B.; Qu, Q. T.; Gao, Q.; Zheng, X. W.; Hub, Z. H.; Wua, Y. P.; Liu, Y. F.; Wang, X. *J. Electrochem. Commun.* **2009**, *11*, 715−718.
(42) Pandolfo, A. G.; Hollenkamp, A. F. *J. Power Sources* **2006**, *157*, 11−27.
(43) McAdarns, E. T.; Lackermeier, A.; McLaughlin, J. A.; Macken, D. *Biosens. Bioelectron.* **1995**, *10*, 67−74.
(44) Moulton, S. E.; Barisci, J. N.; Bath, A.; Stella, R.; Wallace, G. G. *Electrochim. Acta* **2004**, *49*, 4223−4230.
(45) Rosca, I. D.; Watari, F.; Uo, M.; Akaska, T. *Carbon* **2005**, *43*, 3124−3131.
(46) Shen, J.; Yang, C.; Li, X.; Wang, G. *ACS Appl. Mater. Interfaces* **2013**, *5*, 8467−8476.